Coordination Chemistry Reviews
196 (2000) 165–195

COORDINATION CHEMISTRY REVIEWS

www.elsevier.com/locate/ccr

Spectroscopic properties and design of highly luminescent lanthanide coordination complexes

G.F. de Sá [a,*], O.L. Malta [a], C. de Mello Donegá [a], A.M. Simas [a], R.L. Longo [a], P.A. Santa-Cruz [a], E.F. da Silva Jr. [b]

[a] *Departamento de Química Fundamental, Universidade Federal de Pernambuco, Cidade Universitária, 50670-901, Recife-PE, Brazil*

[b] *Departamento de Física, Universidade Federal de Pernambuco, Cidade Universitária, 50670-901, Recife-PE, Brazil*

Received 11 September 1998; received in revised form 7 January 1999; accepted 20 January 1999

Contents

* Corresponding author. Tel.: +55-81-271-8441; fax: +55-81-271-8442.
E-mail address: 41gfs@npd.ufpe.br (G.F. de Sá)

PII: S0010-8545(99)00054-5

Abstract

In this paper recent advances in the development of efficient light conversion molecular devices (LCMD) based on lanthanide complexes are reviewed, with emphasis on the work of our group. We have adopted a strategy based upon both theoretical and experimental (synthesis and methodological) investigations. The theoretical aspects are described in terms of the well known theory of 4f–4f transitions and a recently developed model of intramolecular energy transfer processes in lanthanide coordination compounds. The necessary structural data (coordination geometries and electronic structures of the organic parts of the compounds) are obtained from a sparkle model also recently developed. The results lead us to achieve a better understanding of the factors determining the quantum yields and other relevant properties of these complexes, establishing the basis of a framework for the modeling of new complexes which are promising LCMDs. In addition, the fluorinated compounds, which are sufficiently volatile and thermodynamically stable, are candidates for a number of applications. We illustrate their use as LCMDs devices for sensing UV radiation (dosimeter) and as antireflection coatings (ARC) on silicon solar cells with beneficial effects on device performance.

Keywords: Lanthanide coordination; Light conversion molecular devices; Fluorinated compounds

1. Introduction

Interest in the photophysical properties of lanthanide ion complexes has grown considerably since Lehn [1] proposed that such complexes could be seen as light conversion molecular devices (LCMDs), coining the term 'antenna effect' to denote the absorption, energy-transfer, emission sequence involving distinct absorbing (the ligand) and emitting (the lanthanide ion) components, thus overcoming the very small absorption coefficients of the lanthanide ions. The design of efficient lanthanide complexes has become an important research goal, being pursued by several groups [2–37,90,94–96,101,105–115], working with many different classes of ligands (e.g. cryptands [4,16], podands [3,4,115], calixarenes [4,13,15,114], macrocyclic ligands [2,3,106–108], β-diketones [12,20,21,27–29,112,113], heterobiaryl ligands [9,10,105], carboxylic acid derivatives [105], terphenyl ligands [90,111], proteins [109], etc.). Most of the complexes investigated emit red or green light (Eu^{3+} and Tb^{3+} luminescence, respectively), but there are also complexes of different Ln^{3+} ions that luminesce in other spectral regions: near-IR (Yb^{3+}, Nd^{3+}, Er^{3+} [18,19,107–109,111,113]), orange (Sm^{3+} [111,112,114]), yellow (Dy^{3+} [111,112,114]), blue (Tm^{3+} [20,21,111]) or near-UV (Ce^{3+} [16], Gd^{3+} [16,17]).

Efficient LCMDs may find several applications, such as luminescent probes in biomedical assays [2–12] and time-resolved microscopy [9], fluorescent lighting [38], luminescent sensors for chemical species (H^+, O_2, halide ions, OH^-) [106], electroluminescent devices [39], UV dosimeters [37], or antireflection coatings for solar cells [36]. Besides the quantum yield of a LCMD, other aspects, such as light output, solubility, volatility, and photo-, thermal- and thermodynamic stabilities, may be critical to many applications, and must also be controlled.

In order to gain insight into the factors which determine the quantum yield and other relevant properties of lanthanide complexes our group has adopted an approach based upon both theoretical and experimental work, analysing qualitative and quantitative aspects [22–35]. Therefore, besides the synthesis and experimental investigation of the photophysical properties of a number of new lanthanide complexes, our group has been successfully developing theoretical models to determine the coordination geometry of a lanthanide complex [31,32,34], the position and nature of the ligand excited states in the complex [31,32,34], the 4f–4f intensity parameters [32], the ligand-to-lanthanide ion energy transfer rates [32], and the luminescence quantum yields [33].

The variety of β-diketones and adducting molecules which are available allowed the study of varying steric and electronic effects on the structure, luminescence, and efficiency of luminescence, which are of particular importance in the context of connecting modern theoretical ideas to discrete complexes. For example, the availability of complexes of known structure has enabled the theories related to band intensities and crystal field parameters to be tested and extended.

The molecular structure determination is the first step in the rationalization and prediction of the luminescent properties of these lanthanide compounds. The combination of the SMLC/AM1 (sparkle model for lanthanide complexes based on Austin model 1) method [50,52] for obtaining molecular structure with semi-empirical methods for electronic spectra calculations, such as the INDO/S–CI (intermediate neglect of differential overlap/spectroscopic–configuration interaction) method [54], has provided a valuable theoretical tool to study the effects of the ligands on the luminescent properties. The energy levels and transition moments, as well as other electronic properties determined by these combined methodologies, have been used to estimate the energy transfer rates between the ligands and the Ln(III) ion, allowing the calculation of the quantum yield for the luminescence processes [57].

Experimental and theoretical results have shown that the quantum yield of a lanthanide complex arises from a balance among the rates of several processes (e.g. ligand $\rightarrow Ln^{3+}$ energy transfer, multiphonon relaxation, back-transfer and crossover to charge-transfer states). The control of these rates, as well as of other relevant physical properties, has been accomplished by a thorough selection of ligands, allowing us to develop some promising LCMDs [24,27–29,33], with high room temperature quantum yields, leading to new applications [36,37].

2. Preparation of new luminescent complexes, their thin films and devices

2.1. Fluorinated β-diketonates

We have investigated a large number of mixed complexes with general formulae $Ln(L)_3B$, where Ln is Eu^{3+} or Gd^{3+}, L is a β-diketone [24,27,28,32–34] (e.g. bzac = 1-phenyl-1,3-butanedione; btfa = 4,4,4-trifluoro-1-phenyl-1,3-butanedione) and B is a Lewis base such as 1,10-phenanthroline (phen), 2,2′-bipyridine (bipy),

2,2′:6′,2″-terpyridine (terpy), and their *N*-oxide derivatives in the expectation that they would be kinetically more stable than their pyridine analogs and possibly present improved luminescence [89]. The hydrated compounds, where water molecules substitute for the B ligands, are also synthesised for comparison. The Gd^{3+} complexes were prepared in order to allow the determination of the ligands energy levels.

The synthetic procedure can be summarized as described below, although it may vary slightly depending on the ligands. Typically, the complexes $Ln(L)_3B$ were prepared by adding 40 ml of a warm ethanolic solution of ligand B (1 mmol) to an ethanolic solution containing 1 mmol of $Ln(L)_3 2H_2O$. The precipitate was filtered, washed with ethanol and dried at 80°C over P_2O_5 under reduced pressure (less than 1 mmHg). The hydrated complexes were prepared by adding 20 ml of an ethanolic solution of L (1 mmol) to 20 ml of a warm (ca. 70°C) aqueous ethanolic solution of $Ln(ClO_4)_3$ (1 mmol) at pH 4–5. The pH was then adjusted to 6.5 with diluted NaOH aqueous solution. After refluxing for 4 h a precipitate was filtered, recrystallized in ethanol and dried at 80°C over P_2O_5 under reduced pressure. The complexes were characterized by elemental analysis and IR vibrational spectroscopy and, in some cases, also by thermogravimetric analysis. The IR vibrational absorption spectra were measured on a Bruker IF566 FTIR spectrophotometer, using KBr pellet and Nujol mull techniques. The analytical and vibrational data are consistent with the proposed formulae. The vibrational spectra provide evidence that the metal ion is coordinated to the ligands via the C=O and N–O groups.

2.2. Thin film and device processing

The $Eu(btfa)_3bipy$ thin films used in the absorption, luminescence and lifetime measurements were prepared by the deposition of the complex on a slide of quartz substrate previously cleaned and degreased to assure proper film adhesion. Films with thickness ca. 30–90 nm were thermally co-evaporated from an alumina crucible onto the quartz substrate surface and photolithographically defined to form rectangular structures with an area of ca. 1 cm^2. The thickness of the films was monitored during deposition by a quartz crystal thickness meter and by posterior ellipsometry measurements at several wavelengths to assure film quality and uniformity. The refractive index of the $Eu(btfa)_3bipy$ thin films was determined by ellipsometry to be 1.61 ± 0.04 at 632.8 nm.

To further test the optical properties of the $Eu(btfa)_3bipy$ thin films as potential candidate for use in silicon devices as antireflection coatings of solar cells, p-n junctions were fabricated using simple fabrication techniques [36]. Silicon wafers (100) p-type oriented (2 in. diameter) of 1 Ωcm resistivity were cleaned following a standard cleaning process [36], except for the last step, where the wafers were immersed in a 3% HF dip solution, prior to furnace loading. The p-n junctions were formed (after diffusion of a high concentration phosphorus silica glass spun onto specific regions of the wafer surface) in a Thermco MB-80 furnace at 1000°C for 70 min to a depth of ca. 1 m. Aluminum films ca. 200 nm

thick were thermally evaporated from a W boat on to the wafer surface, and photolithographically defined to form circular gates with area of 1×10^{-4} cm^2, within the effective solar cell area of 1×10^{-2} cm^2. After backside metallization, the wafers were annealed in forming gas at 400°C for 30 min. The solar cells were characterized in a HP 4155A Semiconductor Parameter Analyser, before and after the $Eu(btfa)_3bipy$ ARC deposition. After initial characterization some solar cells were covered by an appropriate $Eu(btfa)_3bipy$ complex thin film deposited by thermal evaporation.

3. Spectroscopic measurements

3.1. Electronic absorption, luminescence and lifetimes

The UV–Vis absorption spectra were recorded with a Perkin–Elmer UV–Vis spectrophotometer Lambda 6 Model 2688–002, using 10^{-4} M ethanolic solutions of the complexes. The bands observed in the absorption spectra of the complexes are ascribed to ligand-centered transitions. UV absorption spectra of the fluorinated complexes were also obtained in the solid state from thin films of thickness ranging from 400 to 600 nm.

The solid state photophysical properties of the complexes (viz. Eu^{3+} quantum yields, luminescence and excited state lifetimes at 300, 77, and in some cases, 4.2 K) were investigated for all the complexes. The luminescence spectra of europium and gadolinium complexes were obtained by scanning a 1 m double-grating Jobin-Yvon U-1000 monochromator. The excitation wavelengths were selected by a 0.25 m Jobin-Yvon H-10 monochromator, using a 150 W Xe–Hg lamp as the excitation source. The light detection was performed by a water-cooled RCA C31034 photomultiplier tube, the photocurrent signal being acquired through a EG&G discriminator model 1182 and digitally stored by a Jobin-Yvon Spectralink interface and a personal computer. This set-up allows for measurements at room temperature (298 K) and 77 K.

The excitation and luminescence spectra of some complexes were also obtained by using a SPEX Fluorolog DM3000F Spectrofluorometer with double-grating 0.22 m SPEX 1680 monochromators, and a 450 W Xe Lamp as the excitation source. This set-up is equipped with an Oxford LF205 liquid Helium flow cryostat, allowing for measurements down to 4.2 K. The spectra are corrected for the instrumental response. Excited state decay time and rise time measurements were performed at 298 K using a pulsed N_2 laser as the excitation source. The luminescence was detected with a modified 1P28 photomultiplier tube, after dispersion through a 0.25 m monochromator. The signal was then analyzed on a fast oscilloscope. The temporal resolution of the overall system is ca. 50 ns.

The emission spectra and decay time measurements for the Gd^{3+} complexes allowed the identification of the lowest ligand triplet state in the complexes. As a representative example, the emission spectrum of $Gd(btfa)_3phenNO$ at 77 K is

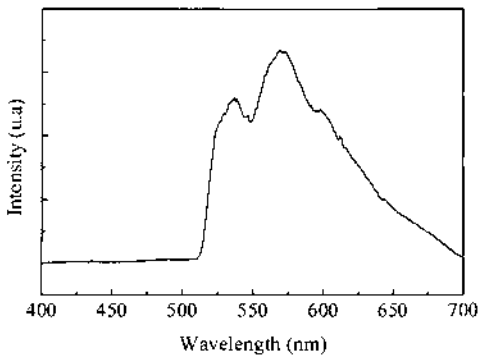

Fig. 1. The emission spectrum of $Gd(btfa)_3phenNO$ at 77 K, upon ligand excitation ($\lambda_{exc} = 370$ nm).

shown in Fig. 1. The ligand phosphorescence is completely quenched at room temperature.

The luminescence spectra of the europium complexes upon ligand excitation consist of Eu^{3+} emission lines only ($^5D_0 \rightarrow {}^7F_J$ transitions, $J = 0$–4). Apart from intensity differences, the spectra are essentially identical at low temperatures. As an example, Figs. 2 and 3 show the luminescence spectra of $Eu(btfa)_3phenNO$ at 300 K and at 4.2 K, respectively. The temperature dependence of the emission intensities can be quite large for some complexes. This will be discussed below, in conjunction with decay times and quantum yields for a few selected complexes.

The excitation spectra of the $^5D_0$ emission of the Eu^{3+} ion in the complexes indicate an efficient ligand-to-metal energy transfer, since the most intense feature in the spectrum is a broad band corresponding to transitions populating ligand-centered excited states (see Figs. 4 and 5).

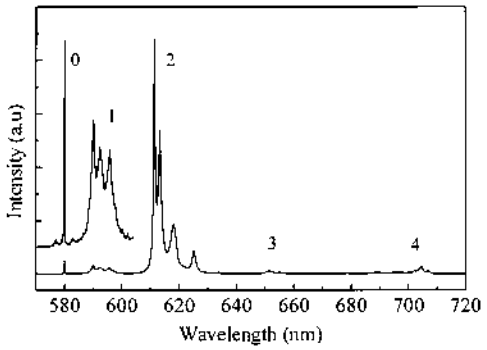

Fig. 2. The luminescence spectrum of $Eu(btfa)_3phenNO$ at 300 K, upon ligand excitation (370 nm). The labels refer to the J values of the final level of the emission transition $^5D_0 \rightarrow {}^7F_J$. The inset shows the $^5D_0 \rightarrow {}^7F_{0,1}$ region magnified.

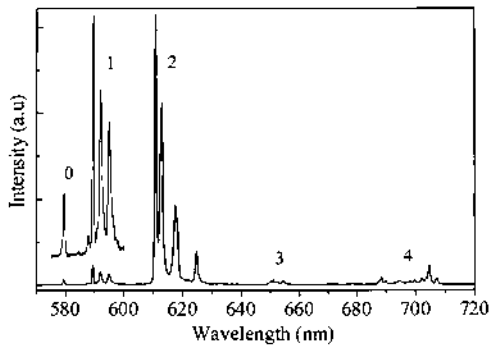

Fig. 3. The luminescence spectrum of $Eu(btfa)_3phenNO$ at 4.2 K, upon ligand excitation (370 nm). The labels refer to the J values of the final level of the emission transition $^5D_0 \rightarrow {}^7F_J$. The inset shows the $^5D_0 \rightarrow {}^7F_{0,1}$ region magnified.

3.2. Quantum yield measurements

The emission quantum yield, q, is defined as the ratio between the number of photons emitted by the Eu^{3+} ion and the number of photons absorbed by the ligand. Following the method developed by Bril and co-workers at Philips Research Laboratories [40–42], the q values for a given sample can be determined by comparison with standard phosphors, whose quantum yields have been previously determined by absolute measurements and are agreed upon. This method is accurate within 10% and provides absolute yields while avoiding absolute measurements. Further, it allows the determination of quantum yields down to 4.2 K, provided the sample is mounted into a cryostat.

The quantum yield q_x of a sample is thus determined as follows:

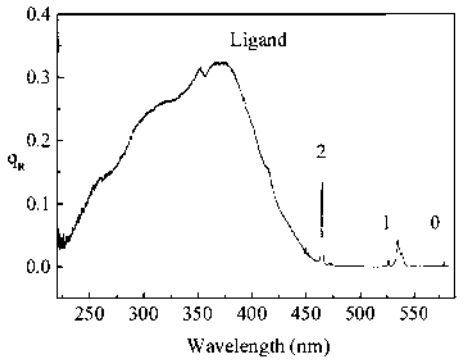

Fig. 4. The excitation spectrum of the $^5D_0$ emission of Eu^{3+} in $Eu(btfa)_3phenNO$ at 300 K. The labels refer to the J values of the final level of the excitation transitions $^7F_0 \rightarrow {}^5D_J$ of Eu^{3+}. q_R gives the relative quantum output.

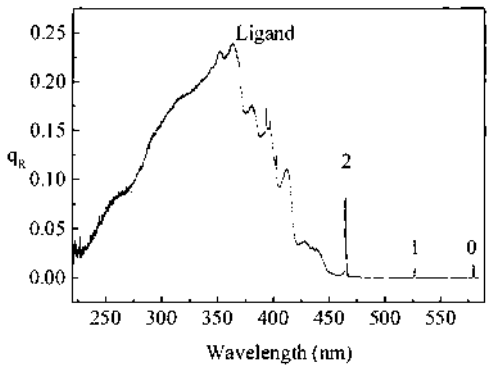

Fig. 5. The excitation spectrum of the $^5D_0$ emission of Eu^{3+} in $Eu(btfa)_3phenNO$ at 4.2 K. The labels refer to the J values of the final level of the excitation transitions $^7F_0 \rightarrow {}^5D_J$ of Eu^{3+}. q_R gives the relative quantum output.

$$q_x = \left(\frac{1 - r_{ST}}{1 - r_x}\right)\left(\frac{\Delta\Phi_x}{\Delta\Phi_{ST}}\right) q_{ST} \tag{1}$$

where r_{ST} and r_x are the amount of exciting radiation reflected by the standard and by the sample, respectively, and q_{ST} is the quantum yield of the standard phosphor. The terms $\Delta\Phi_x$ and $\Delta\Phi_{ST}$ give the integrated photon flux (photons s^{-1}) for the sample and the standard phosphor, respectively. A detailed description of this method has been presented elsewhere [24,25,33]. The quantum yields of some selected complexes will be discussed later in this paper.

4. Modeling of lanthanide complexes

4.1. Structural optimization: the sparkle model for the calculation of lanthanide complexes Austin model 1

The design of new ligands capable of forming stable and highly luminescent lanthanide complexes requires a theoretical model to predict all details of their geometric structure. Molecular mechanics attempts at modeling lanthanide complexes were successfully carried out [43,44] and, due to their fast computation, proved especially useful in molecular dynamics simulations exemplified in the pioneer work of Fossheim et al. [44,45]. However, molecular mechanics approaches possess many deficiencies: they completely disregard the electronic structure of the ligands, and require a different set of parameters for each ligand type and for each central ion which, together with their likely unavailability for the complex being studied, force the researcher to rely on much slower quantum chemical calculations on fragments of the ligands.

Indeed, in spite of the fact that molecular mechanics calculations are fast, provided one has parameters, only relatively few large ligand lanthanide complexes have been studied as in the papers by Ferguson et al. in which they studied three

complexes of coordination number 7 (two of Eu(III) and one of Yb(III)) [43,48]; by Fossheim and co-workers in which they modeled four Gd(III) complexes of coordination number 9 [45] and nine more of such Gd(III) complexes with ligands somewhat similar to the previous ones [44].

Accordingly, we decided to propose a theoretical model for the quantum chemical calculation of lanthanide complexes. We proposed our model within the context of the Austin model 1 semi-empirical molecular orbital introduced by Dewar et al. [46] which is a widely used method mostly in theoretical organic chemistry. We opted for AM1 in order to use its predictive power for the description of the interactions both within and across the organic ligands.

The next step was to develop a model for the lanthanide ion and parameterize it in harmony with all other parameters extant in AM1. In considering what such a model could be, the first question that comes to mind is the role of the f-orbitals in the lanthanide ion: how important are they? Certainly they are essential for the description of the spectroscopic properties of the complex. But are they really important for the prediction of the geometry of a lanthanide complex? Should we include them explicitly within AM1 or not?

Zerner and co-workers [47] used f-orbitals explicitly within INDO and obtained good results for the geometries of small lanthanide complexes. They concluded that f-orbitals do contribute to the pyramidal lanthanide trihalides as well as to the bent structures of the dihalides. On the other hand, they found that for the twelve coordinated complex $[Ce(NO_3)_6]^{2-}$, f-orbital participation does not seem to be significant: 'a stable complex near T_h symmetry is obtained regardless of the f-orbital interaction . . . the large coordination number seems to be a consequence of the relatively large size of the lanthanide ion' [47].

Likewise, molecular mechanics studies have shown that the geometries of lanthanide centers of high coordination number 'are determined largely by ligand–ligand interaction' [43,48]. Indeed, appropriate force field models that describe the most common geometries of lanthanide coordination compounds are those based on inter-ligand interaction using only non-bonded parameters to describe the interaction between ligand and cation [44,45].

From all these studies and also from our own scientific experience with such complexes, a picture for the lanthanide ion begun to emerge as almost purely ionic and therefore electrostatically controlled. Hence, within AM1 it should be described by a central model potential, Coulomb-like in the long range and repulsive in the short range to accommodate the size of the lanthanide ion. This model potential should handle the complexes without demanding excessive computational facilities, bypassing the known difficulties extant in the theoretical treatment of f elements [49]. The model potential that we first proposed for the semi-empirical molecular orbital calculation of lanthanide ion complexes was the sparkle model [50].

Sparkles are used in semi-empirical calculations to represent pure ionic charges, somewhat equivalent to common chemical entities such as Ba^{2+}, $[N(CH_3)_4]^+$, K^+, Cs^+, BH_4^-, X^-, where X stands for a halogen, NO_3^-, SO_4^{2-} or $C_2O_4^{2-}$. In MOPAC 6.00 [51] they all have an ionic radius of 0.7 Å, an integer nuclear charge ($+2$, $+1$, -1 or -2 according to the chemical entity they are to represent), zero

heat of atomization, no orbitals and no ionization potential. Consequently, sparkles cannot accept or donate electrons. They have been designed to serve as counter ions, to create dipoles in a calculation so that they can mimic solvent effects, or to create an electric field from which polarizabilities can be easily calculated. A sparkle, however, is not a point charge ready to collapse with the first opposite sign charge it finds. A more accurate visualization should be of a charge de-localized over the surface of a sphere, such that a pair of opposite sign sparkles resemble a pair of ions forming an ionic bond. Within MOPAC, a sparkle is an integer charge at the center of a repulsive spherical potential of the form $\exp(-\alpha r)$, where α defines the hardness of the sphere in order to prevent the approach of another atom or ion closer to a certain distance.

Our first sparkle model was constructed for europium and consisted of a sparkle charge of exactly $+3$ (to represent the $+3$ lanthanide ions), with parameters ALPAM1 and AMAM1 of subroutine block.f in MOPAC 6.00, both equal to 2.00 and EHEAT equal to $+1005.3$ kcal mol^{-1}. ALPAM1 is α as mentioned in the previous paragraph and AMPAM1 is the monopole–monopole interaction parameter involved in the core–core repulsion integrals. To obtain these parameters we have used the known geometry of the complex tris(acetylacetonate) (1,10-phenantroline) of europium (III). Interatomic distances for the coordination polyhedron, averaging 2.81 Å, could be predicted with an average deviation of 0.13 Å [50].

We then applied this sparkle model to complexes of coordination number 9 and tested our sparkle model predicting the known geometry of the monocrystal tris(dipivaloylmethanato)(2,2′:6,2″-terpyridine) of europium (III), a complex with 126 atoms. Considering its coordination polyhedron, the interatomic distances averaging 2.83 Å and the bond angles could be predicted with an average deviation of 0.12 Å and 5°, respectively, thus reinforcing the validity of our model [52].

In order to improve the model further and at the same type keep it consistent with the AM1 Hamiltonian, our sparkle model has been generalized so that Gaussian functions, similar to the ones used in AM1 to improve the core–core interaction were introduced and all six Gaussian parameters were optimized for several europium(III) compounds [34]. We have only obtained a proper description of complexes with cryptate- and cage-like ligands with the latter parameterization.

With that latter parameterization, more recently, we calculated the geometries of 2,2′-dipyridyl adducts of two europium β-diketonate complexes, $Eu(btfa)_3 \cdot bipy$, where btfa stands for 4,4,4-trifluoro-1-phenyl-2,4-butanedione and bipy stands for 2,2′-dipyridyl, and $Eu(bzac)_3 \cdot bipy$, where bzac stands for 1-phenyl-2,4-butanedione, and compared the output with the crystal structure of the former which we obtained by single-crystal X-ray diffraction methods. The average predicted values for the Eu–O and Eu–N distances are 2.38 and 2.54 Å, and the average deviation of all eight values from the experimental ones in the solid state is 0.05 Å. The data for the bond angles show a similarly good agreement [34].

In conclusion, SMLC/AM1 is a very powerful addition to the semi-empirical molecular orbital method AM1 in that it allows the prediction of geometric parameters of lanthanide complexes of very difficult experimental determination.

4.2. Theoretical model for the electronic spectra of the organic part of the complexes—INDO/S–CI method

Once the molecular structure of the lanthanide complex has been established, the next step towards the design of new luminescent compounds would be the study of the donor (ligands) energy transfer states. This implies in the calculation of the ligand excited states, namely, energy levels and transition moments. In order to provide a realistic model, these calculations should be performed at the ground state geometry of the lanthanide compound, since the excited states are highly dependent upon the chemical environment. For instance, the calculated electronic spectra of the ligands in the complex are very distinct from those of the free ligands ones [53]. In addition, the effects of including the point charge representation of the central ion are quite significant in the energy levels and transition moments within the ligands. Certainly, a complete quantum description of the central ion would be ideal, since it would allow for studies about the covalence effects on the excited states, as well as, the charge transfer excitation bands. However, as it will be outlined below, the energy transfer model employed in our treatment describes the ligands and the central ion separately, on the basis that the excited states of the lanthanide ion are shielded against the molecular environment, and that the main effect of this central ion on the ligands is electrostatic. As a result, the main concern about excited states is with those of the ligands in their mutual presence and affected by a point charge centered at the lanthanide position.

The intermediate neglect of differential overlap/spectroscopic–configuration interaction (INDO–CI) method [54] implemented within the ZINDO program [55] has been successfully employed in the calculation of the energy levels and transition moments of several lanthanide compounds [31,32,34,56–58]. The molecular structure has been obtained as described above (Section 4.1), from the SMLC2/AM1 with the sparkle representing the metal ion being replaced by a point of charge $+3e$ [53]. The CI (configuration interaction) matrix is constructed with configurations generated by all single substitutions on the reference determinant, within a chosen set of occupied and unoccupied orbitals. The choice of this orbital set and the comparison between the observed and the calculated spectra are described in details elsewhere [34,53,56]. Briefly, this orbital set is gradually expanded until there is no visual differences between the spectra generated by two consecutive orbital sets in the observed frequency range. The line broadening of the calculated transition energies and moments is take into account by fitting them to a Van Vleck-Weisskopf [59] or a Lorentzian [60] line shape function with a half-height band width of 20–30 nm, which properly allows the comparison between the calculated and the observed absorption electronic spectra.

The application of the above methodology has been quite successful in explaining qualitative or even quantitative features of the electronic structure of lanthanide compounds as well as the energy transfer rates and quantum yields [31,32,34,56–58]. For instance, the electronic absorption spectra of several Eu(III) complexes, $Eu(apzca)_3 \cdot o$-phen [57], $Eu(picno)_3 \cdot$ terpy [53], $Eu(btfa)_3 \cdot$ bipy [56], $Eu(bzac)_3 \cdot$ bipy [34,58], etc., have been measured and the calculations show a very good agreement, despite the neglect of the solvent effects [31,53].

In general, the calculated spectra are blue shifted by 10–30 nm relative to the observed ones [31,34,58]. However, not only the energy levels are important, but also the transition moments are a significant ingredient of our model for calculating energy transfer rates. Thus, a reliable theoretical approach should also provide (relative) intensities in good agreement with the experimental results. This has also been accomplished by the present methodology to calculated excited states, not only for reproducing qualitative and quantitative features of the observed electronic spectra [31,32,34,53,56–58], but also in providing accurate values for energy levels and transition moments that allows the calculation of transfer rates that are consistent to the observed quantum yield [31,32,34,56–58].

The triplet energy levels are also very important in the energy transfer model, and they are not probed by the electronic absorption spectroscopy. Thus, using phosphorescence spectroscopy the triplet energy levels of several Gd(III) compounds [32,61] have been probed allowing for the test of the accuracy of the calculated triplet states. It should be noted that the calculated lowest triplet energy level for these Gd(III) compounds is in perfect qualitative agreement with the observed data, and the quantitative agreement is also very good since it is off by at most 5% from the experiment [32,62]. These results show then the reliability of this methodology to yield information about the ligand excited states in lanthanide compounds, encouraging us to apply it to several other systems such as macrocyclic cage-like ligands and polymeric systems doped with rare earth metal ions. The calculated structures of cage-like bpy · bpy · bpy cryptate ligands and their *N*-oxide derivatives have corroborated the experimental evidence [4] that the oxidation of the nitrogen atom leads to a loss of coordinated water molecule [63]. In addition, the calculated absorption electronic spectra are good agreement with the observed ones and the calculated triplet energy levels [63] seems to correlate quite well with the measured emission efficiency [4] of several Eu(III) compounds.

The condensation of phthalic acid and ethylene glycol with small amounts of heteroaromatic acids yields a polymeric system, which is characterized by relatively small (10–15 units) chains since the heteroaromatic acids act as terminators. Rare earth metal ions have been used as spectroscopic and structural probes of these polymeric systems. In order to obtain the most information from this probing, it would be important to have an approximate structure of Eu(III) coordinated to the doped polymer. Several possible structures have been calculated [64] and one of them is shown in Fig. 6, which corresponds to a complex with seven monomeric units and one heteroaromatic residue. The calculated electronic absorption spectrum agrees qualitatively quite well with the observed one (Fig. 7), including the structure appearing at the top of the band. It has been proposed that the most prominent spectroscopic feature of this system is the formation of exciplexes due to the charge transfer transition within the polymer chain [65]. The calculated excited states corroborates this assertion, however, in the case of the polymer in the presence of the lanthanide ion the exciplex is formed between two nearby aromatic rings belonging to different chain and coordinate to the metal ion [64].

These methodologies have achieved a high degree of applicability ranging from the semi-quantitative explanation of the substituent effects ($CH_3 \rightarrow CF_3$) on the

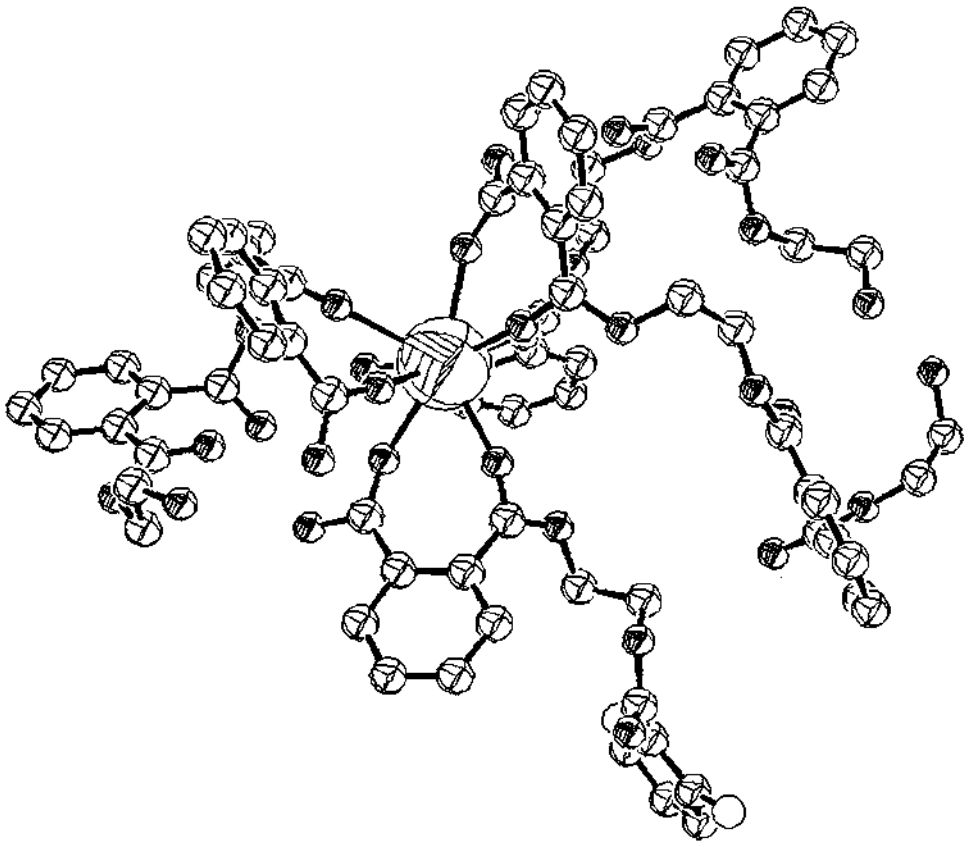

Fig. 6. Calculated structure of the Eu(III) coordinated to three dimeric units of polyethylene phthlate (PET) and one unit of (PET) terminated by an amine-3-pyridine-2-carboxylic acid.

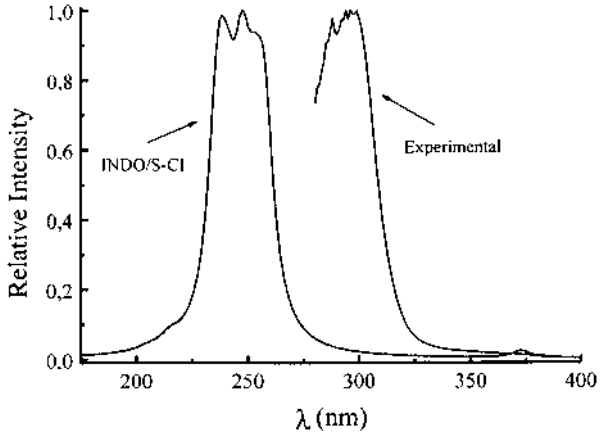

Fig. 7. Experimental spectrum of polyethylene phthlate (PET) doped with amine-3-pyridine-2-carboxylic acid and Eu(III) ion, and the calculated electronic absorption spectrum of the structure shown in Fig. 6.

luminescence efficiencies (16%→65%) [34] to the calculation of emission quantum yield of several lanthanide compounds [33], and thus, just a step shorter from the design of new LCMD.

4.3. 4f–4f intensities

The characteristic absorption and emission spectra of lanthanide compounds in the visible, near ultra-violet and near infra-red is attributed to transitions between 4f levels due to the fact that they present sharp lines, specially at low temperature, with oscillator strengths typically of the order of 10^{-6}. These transitions are electric dipole forbidden to first-order, but are allowed by the electric quadrupole, vibronic, magnetic dipole and forced electric dipole mechanisms [66]. It has been known for more than 50 years, that among these mechanisms only the magnetic dipole and forced electric dipole ones could account for the observed intensities [67]. The magnetic dipole character of the $^5D_0 \rightarrow {}^7F_1$ transition of the Eu^{3+} ion was demonstrated in 1939 by Deutschbein [68]. Most of the 4f–4f transitions in the lanthanide series, however, cannot be accounted for by the magnetic dipole mechanism, not only because the predicted oscillator strengths are in general smaller than 10^{-6} but also due to the restrictive selection rules on the total angular momentum quantum number J, $|\Delta J| = 0, 1$ ($0 \leftrightarrow 0$ excluded), as far as J is considered to be a good quantum number.

The forced electric dipole mechanism was treated in detail for the first time in 1962 by Judd [69] and Ofelt [70] through the powerful technique of irreducible tensor operators [71–73]. Two years later it was proposed by Jørgensen and Judd [74] that an additional mechanism of 4f–4f transitions, originally referred to as the pseudoquadrupolar mechanism due to inhomogenieties of the dielectric constant, could be as operative as, or, for some transitions, even more relevant than, the forced electric dipole one.

In the standard theory the integrated coefficient of spontaneous emission of a transition between two manifolds J and J' is given by

$$A_{JJ'} = \frac{4e^2\omega^3}{3\hbar c^3}\left[\frac{n(n^2+2)^2}{9} S_{\mathrm{ed}} + n^3 S_{\mathrm{md}}\right] \tag{2}$$

where ω is the angular frequency of the transition, e is the electronic charge, c is the velocity of light, $\hbar$ is Planck's constant over 2π and n is the refractive index of the medium. The electric and magnetic dipole strengths, respectively, S_{ed} and S_{md} (in units of e^2), are given by

$$S_{\mathrm{ed}} = \frac{1}{(2J+1)} \sum_{\lambda=2,4,6} \Omega_\lambda \langle J' \| U^{(\lambda)} \| J \rangle^2 \tag{3}$$

where the quantities Ω_λ are the so-called Judd–Ofelt intensity parameters [69,70], and

$$S_{\mathrm{md}} = \frac{\hbar^2}{4mc^2} \langle J' \| L + 2S \| J \rangle^2 \tag{4}$$

where m is the electron mass. The reduced matrix elements appearing in Eqs. (3) and (4) are evaluated in the intermediate coupling scheme [66], and the angular momentum operators L and S are in units of $\hbar$. The corresponding expression for the oscillator strength may be obtained from the relation

$$P_{JJ} = \frac{2J+1}{2J'+1} \frac{mc^2}{2\omega^2 e^2 n^2} A_{JJ} \tag{5}$$

The intensity parameters Ω_λ depend on both the chemical environment and the lanthanide ion, and theoretically they are given by

$$\Omega_\lambda = (2\lambda+1) \sum_{t,p} \frac{|B_{\lambda tp}|^2}{(2t+1)} \tag{6}$$

where the quantities $B_{\lambda tp}$, which have been described in detail elsewhere [75,76], may be expressed as

$$B_{\lambda tp} = \frac{2}{\Delta E} \langle r^{t+1} \rangle \theta(t, \lambda) \gamma_p^t - \left[\frac{(\lambda+1)(2\lambda+3)}{(2\lambda+1)} \right]^{1/2} \langle r^\lambda \rangle (1-\sigma_\lambda) \langle 3 \| C^{(\lambda)} \| 3 \rangle \Gamma_p^t \delta_{t,\lambda+1} \tag{7}$$

where ΔE is the energy difference between the barycenters of the excited $4f^{N-1}$ 5d and ground $4f^N$ configurations, $\langle r^x \rangle$ is a radial expectation value, $\theta(t, \lambda)$ is a numerical factor, σ_λ is a screening factor, $C^{(\lambda)}$ is a Racah tensor operator of rank λ and $\delta_{t,\lambda+1}$ is the Kronecker delta function. The first term in the right-hand-side of Eq. (7) corresponds to the forced electric dipole mechanism, as expressed by the average energy denominator method, and the second term corresponds to the dynamic coupling mechanism within the point dipole isotropic ligand polarizability approximation.

The sums-over-ligands γ_p^t, the so-called odd-rank ligand field parameters, and Γ_p^t ($t = 1, 3, 5$ and 7) contain the dependence on the coordination geometry and on the nature of the chemical environment around the lanthanide ion. The latter one is given by

$$\Gamma_p^t = \left(\frac{4\pi}{2t+1} \right)^{1/2} \sum_j \frac{\alpha_j}{R_j^{t+1}} Y_p^{t*}(\theta_j, \varphi_j) \tag{8}$$

where α_j is the isotropic polarizability of the jth ligand atom, or group of atoms, at position $\vec{R}_j$ and Y_p^t is a spherical harmonic of rank t. Anisotropic corrections to Eq. (8) have been discussed in ref. [77]. Among the existing ligand field models in the literature we have systematically applied the simple overlap model developed in our group [78]. According to this model the ligand field parameters γ_p^t are expressed as

$$\gamma_p^t = \left(\frac{4\pi}{2t+1} \right)^{1/2} e^2 \sum_j \rho_j (2\beta_j)^{t+1} \frac{g_j}{R_j^{t+1}} Y_p^{t*}(\theta_j, \varphi_j) \tag{9}$$

where ρ_j is the magnitude of the total overlap between 4f and ligand wavefunctions and $\beta_j = 1/(1+\rho_j)$. Eq. (9) should be interpreted as a ligand field parameter produced by effective charges—$\rho_j g_j e$ located around the mid-points of the lanthanide–ligand chemical bonds. Thus, the charge factors g_j are more appropriately treated as parameters which no longer have to be given by the valencies of the ligand atoms. The overlap ρ_j has been assumed to vary as

$$\rho_j = \rho_0 \left(\frac{R_0}{R_j} \right)^n \tag{10}$$

where R_0 is the smallest among the R_js, $\rho_0 = 0.05$ and $n = 3.5$ [76]. The even rank ligand field parameters, which give the Stark splitting of the J manifolds, are given by their usual expression $B_q^k = \langle r^k \rangle \gamma_q^k$.

It might be useful to consider the heat of formation, Q, of a coordination compound, associated with the reaction

$$\text{Ln ion} + x\text{L}_1 + y\text{L}_2 \rightarrow \text{Ln}(\text{L}_1)_x(\text{L}_2)_y$$

According to the simple overlap model this is given by [32]

$$Q = -3e^2 \sum_j g_j \rho_j \frac{2\beta_j}{R_j} \tag{11}$$

where the sum runs over the $x\text{L}_1$ and $y\text{L}_2$ ligating atoms. The value of Q gives information on the stabilization energy of the compound.

In the theoretical analysis of 4f–4f intensities two procedures may be adopted. One is to take the charge factors g_j as the valencies of the ligating atoms, and the polarizabilities α_j from data available in the literature [79]. The other one is to take these quantities as variable parameters within ranges of physically acceptable values [32,76]. The usefulness of a theoretical analysis is that it allows one to distinguish between the forced electric dipole and dynamic coupling mechanisms, and as a consequence one may in principle get detailed information on the chemical environment around the lanthanide ion. Moreover, it also allows the rationalization of certain features of the 4f–4f spectra as, for example, in the case of the behavior of the so-called hypersensitive transitions, which has been interpreted in terms of the dependence of the dynamic coupling mechanism on the coordination geometry and on the polarizabilities of the ligands [80].

As the site occupied by the lanthanide ion becomes more symmetric, the lower rank γ_p^t and Γ_p^t tend to vanish more rapidly than the higher rank ones, or in a more general way, the former quantities are more sensitive to changes in symmetry than the latter ones, though the higher rank γ_p^t and Γ_p^t are more sensitive to changes in distances. This goes in the correct sense towards the understanding of the behavior of the hypersensitive transitions, which are in general those dominated by the effective operator $\Omega_2 U^{(2)}$. However, it has been observed that symmetry alone cannot account for the enormous variation sometimes observed in the intensities of these transitions for different chemical environments. Theoretical estimates have shown that the dynamic coupling contribution is able to account for this enormous intensity variation through the polarizabilities of the ligating atoms, or groups of

atoms. Thus, for example, in going from the gaseous compound NdF_3 to gaseous NdI_3, there is a change in polarizability, from the ion F^- to the ion I^-, of almost one order of magnitude. This might produce a change of almost two orders of magnitude in the intensities dominated by $\Omega_2 U^{(2)}$. Abnormal changes in the intensities dominated by $\Omega_4 U^{(4)}$ and $\Omega_6 U^{(6)}$ may not occur since for these cases the considerable increase in the distance Nd–L (L = F and I) may compensate for the increase in the polarizability value.

In Table 1 we present the experimental and theoretical intensity parameters for several Eu^{3+} complexes with β-diketones. The Ω_6 parameter was not determined since the $^5D_0 \rightarrow {}^7F_6$ transition could not be detected. It occurs in the near IR (~ 840 nm) and thus beyond the detection range of our experimental setup. The experimental values of Ω_2 and Ω_4 were determined from the $^5D_0 \rightarrow {}^7F_2$ and $^5D_0 \rightarrow {}^7F_4$ transitions, respectively, by taking the magnetic dipole transition $^5D_0 \rightarrow {}^7F_1$ as the reference [32,76]. The theoretical values were calculated from the structural data obtained from the sparkle model described in the previous subsections. The optimum values of charge factors and polarizabilities, also presented in Table 1, were obtained by including in the fitting procedure the maximum splitting of the $^7F_1$ level and the ratio between the intensities of the $^5D_0 \rightarrow {}^7F_0$ and $^5D_0 \rightarrow {}^7F_2$ transitions, as done in refs. [32,76].

Table 1
Experimental and theoretical 4f–4f intensity parameters, charge factors and polarizabilities (optimum values) for some Eu^{3+} complexes[a]

Compound[b]		Intensity parameter (10^{-20} cm^2)		Charge factor		Polarizability (Å^3)	
		Ω_2	Ω_4	$g(1)$	$g(2)$	$\alpha(1)$	$\alpha(2)$
$Eu(Btfa)_3 2H_2O$	Exp.	20.60	3.50				
	Theor.	20.60	3.10	0.75	1.17	2.53	5.19
$Eu(Btfa)_3$*o*-phenNO	Exp.	28.50	3.90				
	Theor.	16.10	5.30	0.30	2.98	3.61	0.30
$Eu(3\text{-}NH_2pic)_3 2H_2O$	Exp.	9.30	3.70				
	Theor.	9.70	3.70	0.30	0.17	2.00	3.50
$Eu(3\text{-}NH_2pic)_3$*o*-phen	Exp.	8.30	5.53				
	Theor.	8.54	3.78	0.37	2.80	0.37	3.90
$Eu(DPM)_3$*o*-phen	Exp.	13.00	4.00				
	Theor.	12.50	2.70	2.00	3.00	3.20	1.50
$Eu(TTA)_3 2H_2O$	Exp.	33.00	4.60				
	Theor.	19.80	4.70	1.00	2.00	4.00	1.00
$Eu(TTA)_3$DBSO	Exp.	29.00	3.50				
	Theor.	25.70	2.50	1.80	1.40	1.80	4.50

[a] For these latter, 1 refers to the β-diketone's oxygens and 2 refers to the oxygens of the H_2O, *o*-phenNO, DBSO and nitrogens of the *o*-phen ligands.

[b] TTA, thenoyltrifluoroacetonate; DBSO, dibenzylsulfoxide; 3-NH_2pic, 3-aminopyridine-2-carboxylic acid; DPM, dipivaloylmethane. Remaining ligands, as defined in Section 2.1.

A point to be noted is the uncommonly high values of the Ω_2 intensity parameter, reflecting the hypersensitive behavior of the $^5D_0 \rightarrow {}^7F_2$ transition when compared to the case of the Eu^{3+} ion in inorganic materials. According to the dynamic coupling mechanism, this indicates that, in these compounds, the Eu^{3+} ion is in a highly polarizable chemical environment, which explains some rather high values of polarizabilities (within a physically acceptable range) presented in Table 1. A more systematic analysis of the trends in the g and α values, including a larger number of compounds, is in progress.

4.4. Intramolecular energy transfer rates

In order to optimize the quantum yield and light output of a LCMD, several processes must be controled: (i) the ligand absorption and internal decay processes; (ii) the efficiency of the ligand-to-metal energy transfer; and (iii) the luminescence efficiency of the metal ion. Step (ii), which is crucial in determining the 4f–4f emission quantum yield, was firstly identified by Weissman in the study of the strong luminescence presented by certain organoeuropium compounds [81]. In spite of the experimental difficulties, a few estimates of transfer rates have been made [82–84]. However, to our notice, no detailed investigation on the ligand–lanthanide ion energy transfer mechanisms, and their associated selection rules, has been carried out. This problem was recently analyzed in refs. [85,86], where both the direct and exchange Coulomb interactions have been taken into account, leading to analytical expressions for the energy transfer rates from which selection rules could be derived.

According to Fermi's golden rule, within the Born–Oppenheimer approximation, the energy transfer rate, W_{ET}, is given by

$$W_{ET} = \frac{2\pi}{\hbar} |\langle \psi' \phi | H | \psi \phi' \rangle|^2 F \tag{12}$$

where ψ and ϕ' are the initial electronic states of the lanthanide ion and of the ligand, respectively. After energy transfer takes place these are found in the electronic states ψ' and ϕ. The temperature dependent factor F contains a sum over Franck–Condon factors and the energy mismatch condition for the transfer process. An approximate expression has been proposed for this factor, which is

$$F = \frac{1}{\hbar \gamma_L} \left(\frac{\ln 2}{\pi} \right)^{1/2} \exp\left[- \left(\frac{\Delta}{\hbar \gamma_L} \right)^2 \ln 2 \right] \tag{13}$$

where γ_L is the ligand state band width at half-height and Δ is the difference between the donor and acceptor transition energies involved in the transfer process. In this expression it is assumed that donor and acceptor transitions have gaussian band shapes and that γ_L is much larger than the lanthanide state band width at half-height.

The following expressions for the transfer rate have been obtained in refs. [85,86]

$$W_{ET} = \frac{2\pi}{\hbar}\frac{e^2 S_L}{(2J+1)G} F \sum_{\lambda} \gamma_\lambda \langle \alpha' J' \| U^{(\lambda)} \| \alpha J \rangle^2 \quad (14)$$

which corresponds to the dipole–2^λ pole mechanism, with $\lambda = 2$, 4 and 6,

$$W_{ET} = \frac{4\pi}{\hbar}\frac{e^2 S_L}{(2J+1)GR_L^6} F \sum_{\lambda} \Omega_\lambda^{ed} \langle \alpha' J' \| U^{(\lambda)} \| \alpha J \rangle^2 \quad (15)$$

corresponding to the dipole–dipole mechanism, also with $\lambda = 2$, 4 and 6, and

$$W_{ET} = \frac{8\pi}{3\hbar}\frac{e^2(1-\sigma_0)^2}{(2J+1)GR_L^4} F \langle \alpha' J' \| S \| \alpha J \rangle^2 \sum_{m} \left| \left\langle \phi \left| \sum_{k} \mu_z(k) s_m^{(k)} \right| \phi' \right\rangle \right|^2 \quad (16)$$

corresponding to the exchange mechanism.

In the above equations J is the total angular momentum quantum number of the lanthanide ion and α specifies the 4f spectroscopic term. G is the multiplicity of the ligand initial state and S_L is the dipole strength associated with the transition $\phi \rightarrow \phi'$ in the ligand. $U^{(\lambda)}$ is the same unit tensor operator which appears in Eq. (3), the reduced matrix elements of which are given in the intermediate coupling scheme [87], and R_L is the distance from the lanthanide ion to the region of the ligand molecule in which the ligand donor (acceptor) state is localized [32]. The quantities Ω_λ^{ed} are the well-known Judd–Ofelt intensity parameters (forced electric dipole contribution only), and the γ_λs are given by

$$\gamma_\lambda = (\lambda+1)\frac{\langle r^\lambda \rangle^2}{(R_L^{\lambda+2})^2} \langle 3 \| C^{(\lambda)} \| 3 \rangle^2 (1-\sigma_\lambda)^2 \quad (17)$$

In Eq. (16), S is the total spin operator of the lanthanide ion, μ_z is the z-component of the electric dipole operator, s_m ($m = 0, \pm 1$) is a spherical component of the spin operator and the index k runs over the electrons of the ligand. σ_0 is a screening factor of the same nature as those appearing in Eqs. (7) and (17) [32]. The matrix element involving the coupled operators μ_z and s_m can be treated by quantum chemical methods in the same way as the spin–orbit interaction is evaluated in molecular systems [32,88]. It has been calculated, in our case, from the molecular orbital wavefunctions obtained with the sparkle model described in Sections 4.1 and 4.2. These ligand wavefunctions also leads to the following definition of R_L

$$R_L = \frac{\sum_i c_i^2 R_L(i)}{\sum_i c_i^2} \quad (18)$$

where c_i is the molecular orbital coefficient of atom i contributing to the ligand donor (or acceptor) state and $R_L(i)$ is the distance from atom i to the lanthanide ion.

The selection rules for the transfer process may be derived from the reduced matrix elements in the above equations. Thus, one finds that $|J - J'| \leq \lambda \leq J + J'$ ($J' = J = 0$ *excluded*), for the multipolar (dipole–2^λ pole and dipole–dipole) mechanisms, and $\Delta J = 0, \pm 1$ ($J' = J = 0$ *excluded*) for the exchange mechanism. It may,

therefore, be noted that these selections rules are complementary. From the ligand side the selection rules are taken into account through the values of S_L and of the ligand matrix element in Eq. (16). Since in this latter the electric dipole operator is coupled with the spin operator, the usual selection rule on the multiplicities of the states ϕ and ϕ' no longer applies. According to these selection rules, in the case of the Eu^{3+} ion, direct energy transfer to the $^5D_0$ level is not allowed. This rule is, however, relaxed due to J-mixing effects and thermal population of the $^7F_1$ level. On the other hand, quenching of emission from this level is allowed provided the Eu^{3+} ion ends up in the $^7F_6$, $^7F_4$, $^7F_2$ or $^7F_1$ levels. Through the multipolar mechanisms, for this ion, good candidates to be involved with the transfer process would be the $^5D_2$, $^5L_6$, $^5G_6$ and $^5D_4$ levels, while through the exchange mechanism a strong candidate would be the $^5D_1$ manifold.

4.5. Rate equations and luminescence quantum yields: theory and experiment

The luminescence quantum yield of a given lanthanide complex is determined by a balance between radiative and non-radiative processes in the compound, and can be estimated by solving a set of appropriate rate equations, involving the transition and energy transfer rates, as well as the populations of the energy levels of both the lanthanide ion and the ligand [33].

However, before estimating the quantum yields for some selected complexes, it is useful also to provide some experimental data for comparison. Table 2 collects the main results for some representative Eu^{3+} complexes. The experimental quantum yields were obtained as described above (Section 3.2). The positions of the lowest

Table 2
Solid state photophysical data for the $^5D_0$ luminescence of some selected Eu^{3+} complexes[a]

Complex[b]	q (%)	R_I	A_{RAD} (s^{-1})	A_{NR}^{300} (s^{-1})	A_{NR}^{77} (s^{-1})	Tripl (cm^{-1})	τ_{TR} (μs)	Refs.
$Eu(trop)_3$	$<10^{-3}$	1	$\sim10^3$	$\geq10^6$	$\geq10^6$	15 630	130	[35]
$Eu_2(sq)_3(H_2O)_8$	0.02	40	$\sim10^3$	$\geq10^5$	$\geq10^4$	23 600	300	[25]
$Eu(bzac)_3 2H_2O$	15	2.5	700	2678	2266	21 797	0.41	[28,92]
$Eu(bzac)_3$phen	18	2.5	673	1748	719	21 583	0.43	[28,92]
$Eu(bzac)_3$phenNO	27	1.07	879	708	496	19 420	0.46	[28,92]
$Eu(btfa)_3 2H_2O$	22	1.42	349	2283	1734	21 595	0.17	[27,92]
$Eu(btfa)_3$ phen	38	–	580	569	566	21 633	0.21	[92]
$Eu(btfa)_3$ phenNO	65	1.14	760	786	737	19 600	0.37	[27,92]
$Eu(tta)_3 2H_2O$	23	–	1110	2740	–	21 280	–	[32,33]
$Eu(tta)_3$2DBSO	85	–	980	420	–	21 280	1300	[32,33]

[a] Quantum yields q upon ligand excitation ($\lambda_{exc} = 370$ nm) at 300 K, the ratio R_I between the integrated $^5D_0$ emission intensities at 77 and 300 K, the $^5D_0$ radiative (A_{RAD}) and non-radiative decay rates at 300 and 77 K (A_{NR}^{300} and A_{NR}^{77}, respectively). The position of the lowest ligand triplet state (Tripl) in the complex and the triplet lifetime (τ_{TR}) at 77 K are also included.

[b] TTA, Thenoyltrifluoroacetonate; trop, tropolone, 2-hydroxy-2,4,6-cycloheptatrien-1-one; sq, squarate, cyclobutenedionate; DBSO, dibenzylsulfoxide. Remaining ligands, as defined in Section 2.1.

ligand triplet states in the complexes correspond to the onset of the highest energy tail of the low temperature emission spectra for the Gd^{3+} complexes (see Fig. 1 for a representative example). The $^5D_0$ radiative decay rates (A_{RAD}) for the Eu^{3+} complexes are obtained by summing over the radiative rates A_{0J} for each $^5D_0 \rightarrow {}^7F_J$ emission transition. The A_{0J} rates were calculated from the intensity ratios between the $^5D_0 \rightarrow {}^7F_J$ and the $^5D_0 \rightarrow {}^7F_1$ emission transitions (I_{0J} and I_{01}, respectively) and the magnetic–dipole transition rate A_{01}, as described in [27]:

$$A_{0J} = A_{01} \frac{I_{0J}}{I_{01}} \frac{v_{01}}{v_{0J}} \tag{19}$$

The magnetic–dipole transition rate A_{01} is estimated to be 50 s^{-1}, following

$$A_{01} = 10^{-42} v^3 n^3 \frac{(L+2S)^2}{g_J} \tag{20}$$

Here the terms $(L+2S)^2$ are the squared matrix elements, taken from ref. [90], g_J is the statistical weight $(2J'+1)$ of the excited state [91], n is the refractive index, and v is the transition frequency.

The non-radiative rates A^T_{NR} can be obtained from the calculated A_{RAD} rates and the experimental decay rates by [27]:

$$1/\tau^T = A^T_{TOT} = A_{RAD} + A^T_{NR}; \tag{21}$$

where τ^T is the $^5D_0$ decay time at temperature T.

The luminescence spectra of the Eu^{3+} complexes are temperature-independent from 300 to 4.2 K, apart from intensity differences. In all cases shown in Table 2, the ligand phosphorescence is observed for the Gd^{3+} complexes, but not for the Eu^{3+} complexes, indicating that energy transfer from the ligand triplet states to Eu^{3+} excited states is quite efficient. Nevertheless, the quantum yields vary from remarkably high to extremely low values (or even total quenching). The reasons for this behaviour will be discussed below.

We turn now to the theoretical estimation of the quantum yields. In our analysis, we have considered two main energy transfer channels: singlet (ligand) $\rightarrow {}^5D_4(Eu^{3+})$ and triplet (ligand) $\rightarrow {}^5D_1(Eu^{3+})$, but we found that only the latter is important in these cases. A schematic energy level diagram showing the energy transfer channels considered is presented in Fig. 8. The $^5D_1$ and the $^5D_4$ levels of the Eu^{3+} ion were chosen due to the selection rules mentioned above and the favourable energy mismatch conditions (energy level positions for Eu^{3+} in LaF_3: $^5D_0 = 17\,293$; $^5D_1 = 19\,027$; $^5D_2 = 21\,483$; $^5D_4 = 27\,586$ cm^{-1} [87], the levels in the complexes being slightly shifted to lower energies, ca. 20–50 cm^{-1}). Thus, if only the triplet (ligand) $\rightarrow {}^5D_1(Eu^{3+})$ energy transfer channel is considered, we get the following set of rate equations for the normalized populations of the levels involved:

$$\frac{d\eta(S_1)}{dt} = -\frac{1}{\tau(S_1)}\eta(S_1) + \phi\eta(S_0) \tag{22}$$

$$\frac{d\eta(T)}{dt} = -\left(W^{(1)}_{ET}\eta(^7F_0) + \frac{1}{\tau(T)}\right)\eta(T) + \phi^{(1)}_{NR}\eta(S_1) + W^{(1)}_{BT}\eta(^5D_1)\eta(S_0) \tag{23}$$

$$\frac{d\eta(^5D_1)}{dt} = -(W_{BT}^{(1)}\eta(S_0) + W_2)\eta(^5D_1) + W_{ET}^{(1)}\eta(^7F_0)\eta(T) \quad (24)$$

$$\frac{d\eta(^5D_0)}{dt} = -\frac{1}{\tau(^5D_0)}\eta(^5D_0) + W_2\eta(^5D_1) \quad (25)$$

$$\eta(^5D_0) + \eta(^5D_1) + \eta(^5F_1) = 1 \quad (26)$$

$$\eta(S_1) + \eta(S_0) + \eta(T) = 1 \quad (27)$$

where the term η represents the normalized level populations and τ is the level lifetime in the absence of energy transfer. Internal conversion from S_1 to S_0 is assumed here to be much less important than the intersystem crossing from S_1 to T and is not taken into account in the above equations. Under this assumption we have $\phi_{NR}^{(1)} \cong 1/\tau(S_1)$. These rate equations can be solved either numerically or analytically. The emission quantum yield q (the ratio between the numbers of emitted and absorbed photons) is given by

$$q = \frac{A}{\phi}\frac{\eta(^5D_0)}{\eta(S_0)}$$

A comparison between the theoretical and the experimental quantum yields for some Eu^{3+} complexes is presented in Table 3. The energy transfer rates from the

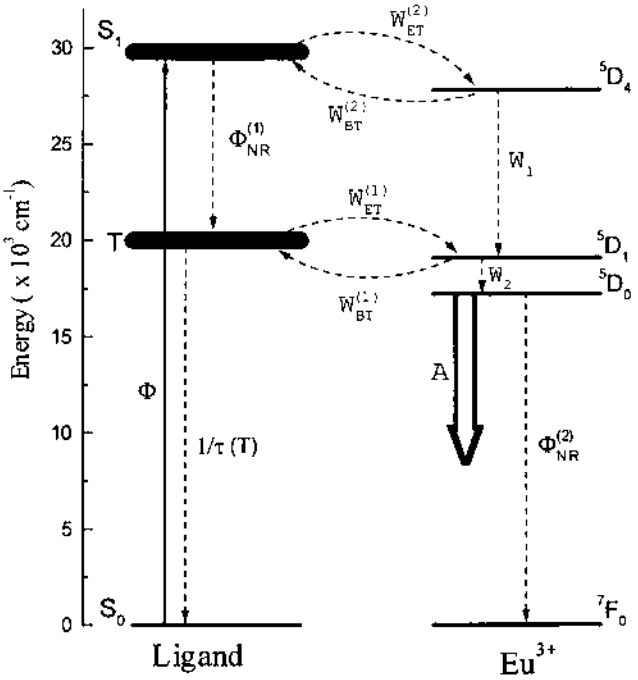

Fig. 8. Schematic energy level diagram for an Eu^{3+} complex showing the most probable channels for the intramolecular energy transfer process.

Table 3
Experimental (q_{EXP}) and theoretical (q_{TH}) quantum yields upon ligand excitation at 300 K for the $^5D_0$ luminescence of some selected Eu^{3+} complexes[a]

Complex	W_{ET} (s^{-1})	W_{BT} (s^{-1})	A (s^{-1})	$\tau^{-1}(^5D_0)$ (s^{-1})	q_{EXP} (%)	q_{TH} (%)	Ref.
$Eu(btfa)_3 2H_2O$	9.9×10^9	8.1×10^9	625	3571	22	19	[92]
$Eu(btfa)_3 phenNO$	2.2×10^{11}	7.4×10^{10}	830	1492	65	56	[92]
$Eu(tta)_3 2H_2O$	1.3×10^9	3.1×10^8	1110	3840	23	29	[33]
$Eu(tta)_3 2DBSO$	7.7×10^8	1.9×10^8	980	1400	85	70	[33]

[a] The rates for the ligand to Eu^{3+} ion energy transfer (W_{ET}) and Eu^{3+} to ligand energy back-transfer (W_{BT}), the Eu^{3+} spontaneous emission coefficients A, and the total decay rates for the $^5D_0$ level of the Eu^{3+} ion ($\tau^{-1}(^5D_0)$) are also included.

ligand triplet state T to the $^5D_1$ level of the Eu^{3+} ion, the back-transfer rates ($^5D_1 \rightarrow T$), the Eu^{3+} spontaneous emission coefficient (equivalent to the A_{RAD} rate), and the total $^5D_0$ decay rates are also given. We assumed a singlet $\rightarrow$ triplet intersystem crossing rate of 10^8 s^{-1}, a triplet state decay rate of 10^5 s^{-1}, and a $^5D_1 \rightarrow {}^5D_0$ non-radiative decay rate of 10^6 s^{-1} [33]. The experimental observation of $^5D_0$ rise-times for many Eu^{3+} complexes (e.g. refs. [27,29]) clearly indicates that the energy transfer from the ligand occurs to the $^5D_1$ level or to levels above it, since the observed rise times correspond to the $^5D_1$ lifetime (i.e. ~ 4 μs).

As mentioned above, the quantum yields upon ligand excitation result from a balance between the ligand to Eu^{3+} energy transfer rates, the $^5D_0$ radiative decay rates A_{RAD}, and the $^5D_0$ non-radiative decay rates A_{NR}. The non-radiative decay rates may have contributions from several non-radiative processes [4,93,95,101]: multiphonon relaxation, energy back-transfer from the lanthanide ion to ligand excited levels, relaxation to the ground state via crossover to another excited state (e.g. the ligand to metal charge-transfer state of the Eu^{3+} ion), or energy transfer between the lanthanide ions themselves. The latter process is usually hampered in complexes, especially between Eu^{3+} ions, due to the rather long Ln–Ln distances (> 5 Å), and can be neglected in our analysis. It must be kept in mind, however, that energy transfer between lanthanide ions can be relevant in many complexes [4,16], particularly for those ions which have longer critical distances for energy transfer (i.e. $r_c > 6$ Å), such as Tb^{3+} or Ce^{3+} [93]. The contribution of the multiphonon relaxation process is essentially temperature independent in the temperature range usually investigated (viz. 4.2–300 K), whereas the rates due to back-transfer or crossover to the Eu^{3+} charge-transfer state are strongly temperature dependent, since these processes are usually phonon-assisted [4,93].

Table 2 presents some examples where the nature of the dominating non-radiative processes can be clearly defined. For instance, the total lack of Eu^{3+} luminescence, even at 4.2 K, in the $Eu(trop)_3$ complex is ascribed to an energy back-transfer to the ligand triplet states, since they are at lower energies than the $^5D_0$ state [30,35]. For the same reason, the $Tb(trop)_3$ complex does not show any luminescence at all [30,35]. Conversely, the strong quenching of the Eu^{3+} emission

in $Eu_2(sq)_3(H_2O)_8$ cannot be due to back-transfer because the ligand states are at much higher energies, and neither can it be due to multiphonon relaxation by coupling to the O–H vibrations since the quenching is strongly temperature dependent [25]. Moreover, the $Tb_2(sq)_3(H_2O)_8$ complex shows a temperature-independent quantum yield of 50% [25]. Therefore, the $^5D_0$ quenching is ascribed to a non-radiative relaxation via the charge transfer (CT) state of Eu^{3+}, which is at rather low energies in the squarate complexes (viz. ca. 20 000 cm^{-1}) [25]. Quenching of the $^5D_0$ emission of Eu^{3+} via a low-lying CT state has also been observed in some cryptates and calixarene complexes [4,12].

A comparison between the complexes of the β-diketones bzac and btfa is worthwhile, since these two ligands are very similar. The btfa complexes have higher quantum yields than bzac complexes and Table 2 clearly indicates that this is due to the lower non-radiative decay rates of the btfa complexes. Considering that the A_{NR} rates are temperature dependent, it can be argued that, besides the multiphonon relaxation by coupling to O–H and C–H vibrations, phonon-assisted back-transfer and/or crossover to the Eu^{3+} CT state are also operative. This latter process probably gives a larger contribution, because the positions of the triplet states for the two classes of complexes seem to be too similar to explain the observed differences. Since the temperature dependence is more pronounced for the bzac complexes, the additional non-radiative process has a larger contribution in this case. The differences between btfa and bzac complexes can be ascribed to the presence of the electron-withdrawing CF_3 group in btfa and the electron-donor CH_3 group in bzac, which would shift the CT state of Eu^{3+} to higher energies. Further, the multiphonon relaxation rates can be reduced (coupling with C–F versus C–H oscillators).

The quantum yields also increase in the sequence $H_2O \rightarrow$ phen $\rightarrow$ phenNO. Table 2 shows that this effect can be ascribed to at least three factors: the A_{RAD} rates increase (probably due to the larger opposite parity admixing induced by the higher polarisability of the ligands), the A_{NR} rates decrease (both the multiphonon relaxation and the temperature dependent rates), and the energy transfer rates increase (due to the lowering of the triplet states leading to better energy mismatch conditions). Table 3 shows that the higher quantum yields of the tta complexes, in comparison with the btfa complexes, are not due to higher energy transfer rates, but rather to larger spontaneous emission coefficients, lower non-radiative rates, and a better balance between energy transfer and back-transfer rates. Finally, it is also important to point out that there is a good agreement between the experimental and the theoretical quantum yields, showing that the theoretical estimation of quantum yields can be a valuable tool for developing efficient LCMDs.

5. Device applications and future developments

In the past decade, luminescent lanthanide complexes have been intensively studied with particular interest towards applications to high efficient LCMDs [94]. A great concern has been the design and successful synthesis of complexes with high

quantum yields, which would also be thermodynamically stable, volatile and compatible with advanced microelectronic technologies for thin film production.

The lanthanide complexes studied in this work embrace a class of new materials that present some of these characteristics, which make them of potential application to a wide range of processes and new technologies. In this section we present the first experimental results on Eu^{3+} and Tb^{3+}-based thin film device structures of great potential for some applications, such as sensors for UV radiation and an antireflection coating (ARC) on silicon solar cells. To our knowledge this is the first time that these complexes are produced as thin films and its optical and photon conversion properties are used to demonstrate the beneficial effects on microelectronic device characteristics. We emphasize here that beyond the high quantum yield of these materials, some new interesting features are obtained, on one hand due to the volatility of most fluorinated β-diketonate complexes and, on the other hand because the control of degradation of some of these complexes, which allows for enlarging the range of applications into electroluminescence devices, dosimeters and advanced microelectronic processes such as photolithography and passivation coatings.

We have produced thin films of Eu^{3+} and Tb^{3+}-based complexes by thermo-evaporation techniques, attaining highly homogeneous films of thickness up to a few hundred Angstroms. For the device applications we have recently envisaged, we used a fluorinated β-diketone, namely btfa (4,4,4-trifluoro-1-phenyl-2,4-butanedione) with 2,2′-bipyridine and 1,10-phenanthroline as heterobiaryl ligands [61]. Two complexes synthesized in recent work [37], $Eu(btfa)_3bipy$ and $Tb(btfa)_3phen$ are very efficient light converters under UV excitation (where the ligands act as excellent antennas, absorbing UV radiation, and efficiently transferring energy to the Ln^{3+} emitters) with a remarkable luminescence quantum yield at room temperature. For instance, the quantum yield for $Eu(btfa)_3bipy$ thin film, measured with an integration sphere, was found to be 64%. The chemical and physical properties of these materials such as thermodynamical stability allow their favorable use comparatively to other volatile ones [102]. In this way, it is possible to thermally evaporate, under low vacuum, fluorinated -diketonate complexes, in order to obtain a highly uniform and stable thin film with strong luminescence comparable to their powder [103] giving it a potential technological applicability.

Using these complexes as UV sensors, the Eu^{3+} red ($^5D_0 \rightarrow {}^7F_2$) and Tb^{3+} green ($^5D_4 \rightarrow {}^7F_5$) emissions were monitored as a function of UV excitation/exposure time for the complex thin films. For the europium species, the red luminescence continuously decreases under UV radiation exposure, which is associated to a controlled ablation of the complex, recently confirmed by ellipsometric measurements [37]. This process is irreversible and was quantified in absolute dose measurements; the luminescence quenching is precisely related to the amount of UV energy per area. In this way, we correlate this ablative process to the UV time exposure and intensity in order to dose, for instance, the cumulative effect of sunlight on human skin. For the $Eu(btfa)_3bipy$ in the powder form, the same behavior is observed, but with a much slower time constant for the luminescence decrease, allowing dosimetric sensitivity control.

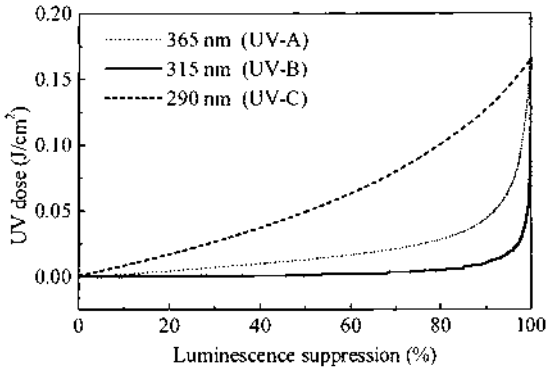

Fig. 9. Dosimetric curves for the device using a 600 Å film for UVA,B and a 150 Å film for UVC.

For the Tb^{3+} $^5D_4 \rightarrow {}^7F_5$ emission, the behavior is opposite for several minutes. A luminescence raise is observed for this green emission, which returns to the initial value afterwards. The system act as a UV dosimeter [104] at a molecular level, and is very selective and sensitive to UV radiation, and may be controlled by varying the film thickness according to the application needs and aims, the source to be measured or the exposed material. The dosimeter was calibrated by an integration sphere coupled to a radiometer.

A curve of energy per unit area (J/cm^2) at the three UV regions regarding skin damage as a function of luminescence quenching is shown in Fig. 9. We may determine the energy per unit area received by the exposed material just by knowing its percentage quenching of luminescence. The dosimeter measurement is done by comparing an UV irradiated sample to a non-irratiated one, therefore, this figure corresponds to the UV dosimeter calibration curve, which may be used to calculate how much UV radiation the material was exposed.

This new kind of UV dosimeter is based on the luminescence decrease of the complexes by UV degradation, and is monitored and correlated to the amount of UV exposure, as shown in the Fig. 9. The effect of the Eu(III) luminescence quenching is reproducible, and is accurately associated with the amount of UV energy per unit area. The greatest advantage of this molecular dosimeter is its wide range of sensitivity that may be adjusted by varying the film thickness allowing us to adjust it to the kind of source to be dosed (artificial or sunlight). The system studied detects the UV radiation in a cumulative way giving it a memory effect, allowing highly reliable dosimetric measurements.

The long-term stability of the $Eu(btfa)_3bipy$ complex in the thin film form has been observed over a 6 month period, exposed to atmospheric pressure, and no noticeable change in its properties was found. All the above characteristics, allied to the compatibility with standard device processing techniques (for thin film production) suggests the possibility of using the material in device applications.

Another simple approach would be its use as antireflection coating (ARC) of photovoltaic devices such as solar cells and photo detectors or sensors associated

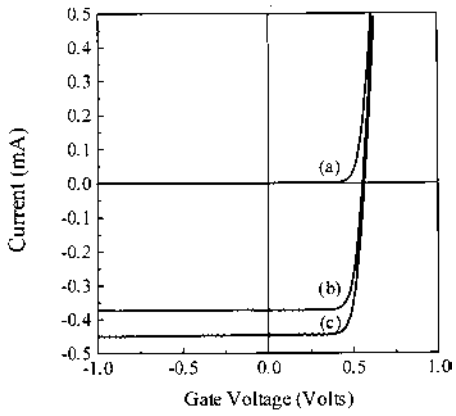

Fig. 10. I × V characteristics of a silicon p-n junction solar cell without and with an antireflection coating (ARC) of Eu(btfa)$_3$bipy thin film of thickness 85.5 nm: (a) dark, no ARC; (b) illuminated, no ARC; and (c) illuminated, with ARC.

with silicon technology. To improve the range of detection for solar cells, for instance, it is possible to use this material as a thin film covering the cell, allowing the detection of the UV radiation by conversion to visible in a highly efficient way, that in addition assures the protection of the cell against UV damage

Fig. 10 illustrates the use of a thin film of the Eu(btfa)$_3$bipy complex deposited over a silicon p-n junction solar cell. Two effects are expected, from this experiment, to affect the solar cell efficiency due to the presence of the thin film: (a) an improvement on efficiency is expected due less reflection of incident light (we refer to the mid-visible spectral range ca. 550 nm for silicon average optical response) when the thin film thickness is equal to $\lambda/4n$, and (b) due to the luminescent properties of the complex some further improvement of the solar cell efficiency is expected as a result of the ultraviolet → visible (red) photon energy conversion as evident from the absorption and luminescent spectra previously discussed. The later is a consequence of the better photon response of silicon cells in the visible, in opposition to the UV spectral region. The curves in Fig. 10 represent the solar cell current–voltage (I × V) characteristics (a) in dark, (b) illuminated without ARC and (c) illuminated with a 85.5 nm thick ARC of the Eu(btfa)$_3$bipy thin film. The improvement obtained in the solar cell efficiency is ca. 21% when the ARC is used. The curve (b) indicate an efficiency of 4.3%, while in curve (c) the efficiency is improved to 5.2% for the same solar cell after the ARC layer deposition. The results presented in Fig. 10 are mainly illustrative and more elaborate optimization in processing is needed for use with higher efficiency solar cell devices produced with more complex cell structures.

The same kind of thermo-evaporated complex may be used in new kinds of self-aligned photolithography processes, due to its compatibility with standard silicon processing technologies, as well as passivating protective coatings.

High efficiency organic electroluminescence devices have recently been important to the development of a new large-size display technologies: 10 years ago, Tang and Slyke demonstrated the viability of low-voltage electroluminescent diodes [97], allowing one to envisage tunability of color in electroluminescent LEDs (light emitting diodes).

The rare earth ions exhibit very sharp emission bands (sharper than usual luminescent organic dyes), allowing a precise color coordinate control, as shown in a new optical material, namely the full color glass, where the three primary light colors are produced only by 4f–4f rare earth emissions [98–100]. The volatility of highly efficient rare earth β-diketonates makes it possible to attain the same process of color control with very narrow emission lines of primary color in mixed thin films or in a multi-layer sandwich of thin films produced by the thermo-evaporation technique.

The new devices obtained by using thin films of fluorinated β-diketonates of lanthanides may improve the quality of color generation for large area displays and solid state microsources of white light. Therefore great interest lies in the possibility of designing dedicated structures for these applications.

Another application of these materials in the film thin form, which we are presently working on, is as electroluminescent LCMDs made of multilayers of different Ln^{3+} complexes. With the use of appropriate metal-contacting carrier injectors, under relatively low biases, could emit light possibly sweeping the full visible range. This would be possible by using multilayer structures of these materials containing Eu^{3+} (red emission), Tb^{3+} (green emission) and Tm^{3+} (blue emission) and taking advantage of the high quantum yield and stability of the complexes in the thin film form.

Acknowledgements

The authors are grateful to CNPq, PADCT, CAPES, FACEPE, and FINEP (Brazilian Agencies) for partially supporting this work, to Dr S. Alves Jr. for spectroscopic measurements, B.J.P. da Silva for technical assistance on the thin film deposition and, Mr Gerd B. da Rocha for providing the calculated triplet results prior to publication.

References

[1] J.-M. Lehn, Angew. Chem. Int. Ed. Engl. 29 (1990) 1304.
[2] M. Pietraszkiewicz, J. Karpiuk, A.K. Rout, Pure Appl. Chem. 65 (1993) 563.
[3] N. Sabbatini, M. Guardigli, I. Manet, R. Ungaro, A. Casnati, R. Ziessel, G. Ulrich, Z. Asfari, J.-M. Lehn, Pure Appl. Chem. 67 (1995) 135.
[4] N. Sabbatini, M. Guardigli, J.-M. Lehn, Coord. Chem. Rev. 123 (1993) 201.
[5] B. Alpha, V. Balzani, J.-M. Lehn, S. Perathoner, N. Sabbatini, Angew. Chem. Int. Ed. Engl. 26 (1987) 1266.
[6] G. Mathis, Clin. Chem. 41 (1995) 1391.

[7] B. Alpha, J.-M. Lehn, G. Mathis, Angew. Chem. Int. Ed. Engl. 26 (1987) 266.
[8] I.A. Hemmilä, Applications of Fluorescence in Immunoassays, Wiley, New York, 1991.
[9] H. Mikola, H. Takkalo, I. Hemmilä, Bioconj. Chem. 6 (1995) 235.
[10] H. Takkalo, V.M. Mukkala, L. Meriö, J.C. Rodriguez-Ubis, R. Sedano, O. Juanes, E. Brunet, Helv. Chim. Acta 80 (1997) 372.
[11] V.M. Mukkala, J.J. Kankare, Helv. Chim. Acta 75 (1992) 1578.
[12] J.-C.G. Bünzli, F. Ihringer, Inorg. Chim. Acta 246 (1996) 195.
[13] J.-C.G. Bünzli, E. Moret, V. Foiret, K.J. Schenk, W. Mingzhao, J. Linpei, J. Alloys Comp. 207/208 (1994) 107.
[14] C. Piguet, G. Bernardinelli, G. Hopfgartner, Chem. Rev. 97 (1997) 2005.
[15] J.-C.G. Bünzli, P. Froidevaux, J.M. Harrowfield, Inorg. Chem. 32 (1993) 3306.
[16] G. Blasse, G.J. Dirksen, N. Sabbatini, S. Perathoner, Inorg. Chim. Acta 133 (1987) 167.
[17] G. Blasse, L.H. Brixner, Recl. Trav. Chim. Pays-Bas 109 (1990) 172.
[18] M.H.V. Werts, J.W. Hofstraat, F.A.J. Geurts, J.W. Verhoeven, Chem. Phys. Lett. 276 (1997) 196.
[19] D.B. Bol'shoi, S.B. Meshkova, Z.M. Topilova, M.O. Lozinskii, Yu.E. Shapiro, Opt. Spectrosc. 83 (1997) 627.
[20] P.K. Sharma, A.R. van Doorn, A.G.J. Staring, J. Lumin. 62 (1994) 219.
[21] E.J. Nassar, P.S. Calefi, I.L.V. Rosa, O.A. Serra, J. Alloys Comp. 275/277 (1998) 838.
[22] G.F. de Sá, W.M. de Azevedo, A.S.L. Gomes, J. Chem. Res. (S) (1994) 234.
[23] G.F. de Sá, F.R.G. e Silva, O.L. Malta, J. Alloys Comp. 207/208 (1994) 457.
[24] C. de Mello Donegá, S. Alves Jr., G.F. de Sá, Chem. Commun. (1996) 1199.
[25] C. de Mello Donegá, S.J.L. Ribeiro, R.R. Gonçalves, G. Blasse, J. Phys. Chem. Solids 57 (1996) 1727.
[26] M.E. Mesquita, G.F. de Sá, M.A.B. Lopes, O.L. Malta, J. Chem. Res. (S) (1996) 120.
[27] C. de Mello Donegá, S. Alves Jr., G.F. de Sá, J. Alloys Comp. 250 (1997) 422.
[28] S. Alves Jr., F.V. Almeida, G.F. de Sá, C. de Mello Donegá, J. Lumin. 72/74 (1997) 478.
[29] M.E. Mesquita, G.F. de Sá, O.L. Malta, J. Alloys Comp. 250 (1997) 417.
[30] B.S. Santos, C. de Mello Donegá, G.F. de Sá, J. Lumin. 72/74 (1997) 535.
[31] A.V.M. de Andrade, N.B. da Costa Jr., R.L. Longo, O.L. Malta, A.M. Simas, G.F. de Sá, Mol. Eng. 7 (1997) 293.
[32] O.L. Malta, H.F. Brito, J.F.S. Menezes, F.R. Gonçalves e Silva, S. Alves Jr., F.S. Farias Jr., A.V.M. de Andrade, J. Lumin. 75 (1997) 255.
[33] O.L. Malta, H.F. Brito, J.F.S. Menezes, F.R. Gonçalves e Silva, C. de Mello Donegá, S. Alves Jr., Chem. Phys. Lett. 282 (1998) 233.
[34] H.J. Batista, A.V.M de Andrade, R.L. Longo, A.M. Simas, G.F. de Sá, N.K. Ito, L.C. Thompson, Inorg. Chem. 37 (1998) 3542.
[35] B.S. Santos, C. de Mello Donegá, G.F. de Sá, L.F.C. de Oliveira, P.S. Santos, Spectrochim. Acta A 54 (1998) 2237.
[36] G.F. de Sá, S. Alves Jr., B.J.P. da Silva, E.F. da Silva Jr., Opt. Mater. 11 (1998) 23.
[37] C.G. Gameiro, E.F. da Silva Jr., S. Alves Jr., G.F. de Sá, P.A. Santa-Cruz, Mater. Sci. Forum (1999) in press.
[38] C.R. Ronda, J. Alloys Comp. 225 (1995) 534.
[39] J. Kido, W. Ikeda, M. Kimura, K. Nagai, Jpn. J. Appl. Phys. 35 (1996) L394.
[40] A. Bril, W. De Jager-Veenis, J. Res. Nat. Bureau Stand. 80A (1976) 401.
[41] A. Bril, W. De Jager-Veenis, J. Electrochem. Soc. 123 (1976) 396.
[42] W. De Jager-Veenis, A. Bril, Philips J. Res. 33 (1978) 124.
[43] D.J. Brecknell, D.J. Raber, D.M. Ferguson, J. Mol. Struct. 124 (1985) 343.
[44] R. Fossheim, H. Dugstad, S.G. Dahl, J. Med. Chem. 34 (1991) 819.
[45] R. Fossheim, S.G. Dahl, Acta Chem. Scand. 44 (1990) 698.
[46] M.J.S. Dewar, E.G. Zoebisch, E.F. Healy, J.J.P. Stewart, J. Am. Chem. Soc. 107 (1985) 3902.
[47] J.C. Culberson, P. Knappe, N. Rösch, M.C. Zerner, Theoret. Chim. Acta 71 (1987) 21.
[48] D.M. Ferguson, D.J. Raber, J. Comp. Chem. 11 (1990) 1061.
[49] D.R. Salahub, M.C. Zerner (Eds.), The Challenge of d and f Electrons. Theory and Computation, American Chemical Society, Washington, 1989.

[50] A.V.M. Andrade, N.B. Costa Jr., A.M. Simas, G.F. de Sá, Chem. Phys. Lett. 227 (1994) 349.
[51] (a) J.J.P. Stewart, J. Comp.-Aided Mol. Des. 4 (1990) 1. (b) M.B. Coolidge, J.J.P. Stewart, MOPAC Manual, Frank J. Seiler Research Laboratory, US Air Force Academy, CO 80840, 1990.
[52] A.V.M. de Andrade, N.B. da Costa Jr., A.M. Simas, G.F. de Sá, J. Alloys Comp. 225 (1995) 55.
[53] A.V.M. de Andrade, R.L. Longo, A.M. Simas, G.F. de Sá, J. Chem. Soc. Faraday Trans. 92 (1996) 1835.
[54] (a) J.E. Ridley, M.C. Zerner, Theor. Chim. Acta 32 (1973) 111; 42 (1976) 223. (b) M.C. Zerner, G.H. Loew, R.F. Kirchner, U.T. Mueller-Westerhoff, J. Am. Chem. Soc. 102 (1980) 589.
[55] M.C. Zerner, ZINDO Manual, QTP, University of Florida, Gainesville, FL 32611, 1990.
[56] H.J. Batista, A.V.M. de Andrade, R.L. Longo, A.M. Simas, G.F. de Sá, L.C. Thompson, J. Lumin. 72/74 (1997) 159.
[57] A.V.M. de Andrade, N.V. da Costa Jr., O.L. Malta, R.L. Longo, A.M. Simas, G.F. de Sá, J. Alloys Comp. 250 (1997) 412.
[58] A.V.M. de Andrade, N.B. da Costa Jr., A.M. Simas, R.L. Longo, O.L. Malta e, G.F. de Sá, Química Nova 21 (1998) 51.
[59] J.H. Van Vleck, V.F. Weisskopf, Rev. Mod. Phys. 17 (1945) 227.
[60] H. Townes, A.L. Schawlow, Microwave Spectroscopy, Dover, New York, 1975.
[61] S. Alves Jr., Ph.D. Thesis, Departamento de Química Fundamental, UFPE, Brazil, 1998.
[62] G.B. da Rocha, Masters Dissertation, Departamento de Química Fundamental, UFPE, Brazil, 1998.
[63] R.L. Longo, IX Brazilian Symp. Theoretical Chemistry, 5, Caxambu, Brazil, 1997.
[64] E.M. Lucena, P.N.M. dos Anjos, R.L. Longo, in preparation.
[65] P.N.M. dos Anjos, W.M. Azevedo, G.F. de Sá, O.L. Malta, J. Lumin. 72/74 (1997) 487.
[66] R.D. Peacock, Struct. Bond. 22 (1975) 83.
[67] L.J.F. Broer, C.J. Gorter, J. Hoogschagen, Physica 11 (1945) 231.
[68] O. Deutschbein, Ann. Phys. 36 (1939) 183.
[69] B.R. Judd, Phys. Rev. 127 (1962) 750.
[70] G.S. Ofelt, J. Chem. Phys. 37 (1962) 511.
[71] B.R. Judd, Operator Techniques in Atomic Spectroscopy, McGraw-Hill Book Company, New York, 1963.
[72] B.L. Silver, Irreducible Tensor Methods: An Introduction for Chemists, Academic Press, London, 1976.
[73] E.U. Condon, H. Odabasi, Atomic Structure, Cambridge University Press, Cambridge, 1980.
[74] C.K. Jørgensen, B.R. Judd, Mol. Phys. 8 (1964) 281.
[75] O.L. Malta, S.J.L. Ribeiro, M. Faucher, P. Porcher, J. Phys. Chem. Solids 52 (1991) 587.
[76] O.L. Malta, M.A. Couto dos Santos, L.C. Thompson, N.K. Ito, J. Lumin. 69 (1996) 77.
[77] J.J. Dallara, M.F. Reid, F.S. Richardson, J. Phys. Chem. 88 (1984) 3587.
[78] O.L. Malta, Chem. Phys. Lett. 88 (1982) 353.
[79] M. Faucher, D. Garcia, Phys. Rev. B 26 (1982) 5451.
[80] B.R. Judd, J. Chem. Phys. 70 (1979) 4830.
[81] S.I. Weissman, J. Chem. Phys. 10 (1942) 214.
[82] G.A. Crosby, Mol. Cryst. 1 (1966) 37.
[83] G.F. Buono-Core, H. Li, B. Marciniak, Coord. Chem. Rev. 99 (1990) 55.
[84] I.M. Alaoui, J. Phys. Chem. 99 (1995) 13280.
[85] O.L. Malta, J. Lumin. 71 (1997) 229.
[86] F.R. Gonçalves e Silva, O.L. Malta, J. Alloys Comp. 250 (1997) 427.
[87] W.T. Carnall, H. Crosswhite and H.M. Crosswhite, Energy level structure and transition probabilities of the trivalent lanthanides in LaF_3, Argonne National Laboratory Report, unnumbered, 1977.
[88] J.T. Yardley, Introduction to Molecular Energy Transfer, Academic Press, New York, 1980, Chap. 7.
[89] A.V.M. de Andrade, M.A. de Brito, A.L. Coelho, G.F. de Sá, Inorg. Chim. Acta 19 (1976) 20.
[90] S. Petoud, J.-C.G. Bunzli, K.J. Schenk, C. Piguet, Inorg. Chem. 36 (1997) 1345.
[91] J.A. Detrio, Phys. Rev. B 4 (1971) 1422.

[92] C. de Mello Donegá, S. Alves Jr., O.L. Malta, G.F. de Sá, Mater. Sci. Forum (1998) in press.
[93] B. Henderson, G.F. Imbusch, Optical Spectroscopy of Inorganic Solids, Clarendon Press, Oxford, 1989.
[94] J.-C Bünzli, G.R Choppin (Eds.), Lanthanides Probes in Life, Medical and Environmental Science, Elsevier, Amsterdam, 1989.
[95] W.W. De Horrocks Jr., D.R. Sudnick, J. Am. Chem. Soc. 101 (1979) 334.
[96] M.P.O. Wolbers, F.C.J.M. Van Veggel, B.H.M. Snellink-Ruel, J.W. Hofstraat, F.A.J. Geurts, D.N. Reinhoudt, J. Am. Chem. Soc. 119 (1997) 138.
[97] C.W. Tang, S.A. Van Slyke, Appl. Phys. Lett. 51 (1987) 913.
[98] J.E.C. da Silva, O.L. Malta, G.F. de Sá, P.A. Santa-Cruz, J. Lumin. 72/73 (1997) 270.
[99] J.E.C. da Silva, O.L. Malta, G.F. de Sá, P.A. Santa-Cruz, Química Nova 21 (1998) 372.
[100] J.E.C. da Silva, O.L. Malta, G.F. de Sá, P.A. Santa-Cruz, Proc. 3rd. Int. Conf. on the Science and Technology of Display Phosphor, CA, November, 3–5, 1997, p. 163.
[101] S.T. Frey, M.L. Gong, W.W. Horrocks De Jr., Inorg. Chem. 33 (1994) 3229.
[102] E.A. Mazurenko, A.I. Gerasimchuk, J. Phys. 4/5 (1995) 547.
[103] K.Z. Wang, Solid State Comm. 98 (1996) 1075.
[104] P.A. Santa-Cruz, C.G. Gameiro, Patent No. PI9705743-6, March, 1998.
[105] G.F. de Sá, L.H.A. Nunes, Z.-M. Wang, G.R. Choppin, J. Alloys Comp. 196 (1993) 17.
[106] D. Parker, P. Kanthi-Senanayake, J.A.G. Williams, J. Chem. Soc, Perkin Trans. 2 (1998) 2129.
[107] A. Beeby, R.S. Dickins, S. Faulkner, D. Parker, J.A.G. Williams, Chem. Commun. (1997) 1401.
[108] A. Beeby, S. Faulkner, Chem. Phys. Lett. 266 (1997) 116.
[109] W.W. Horrocks De Jr., P. Bolender, W.D. Smith, R.M. Supkowski, J. Am. Chem. Soc. 119 (1997) 5972.
[110] S.T. Frey, C. Allen Chang, J.F. Carvalho, A. Varadarajan, L.M. Schultze, K.L. Pounds, W.W. De Horrocks Jr., Inorg. Chem. 33 (1994) 2882.
[111] M.P. Oude Wolbers, F.C.J.M. Van Veggel, B.H.M. Snellink-Ruel, J.W. Hofstraat, F.A.J. Geurts, D.N. Reinhoudt, J. Chem. Soc. Perkin Trans. 2 (1998) 2141.
[112] D.J. Qian, H. Nakahara, K. Fukuda, K.-Z. Yang, Langmuir 11 (1995) 4491.
[113] M. Inamura, Y. Hasegawa, Y. Wada, K. Murakoshi, T. Kitamura, N. Nakashima, T. Yamanaka, S. Yanagida, Chem. Lett. (1997) 1067.
[114] R. Ludwig, H. Matsumoto, M. Takeshita, K. Ueda, S. Shinkai, Supramol. Chem. 4 (1995) 319.
[115] P.L. Jones, A.J. Amoroso, J.C. Jeffery, J.A. McCleverty, E. Psillakis, L.H. Rees, M.D. Ward, Inorg. Chem. 36 (1997) 10.